Scientific Reports

https://doi.org/10.1038/s41598-026-65156-6

Article in Press

Label-free holotomographic imaging of brain myelin

Received: 26 August 2025

Accepted: 29 July 2026

Published online: 20 August 2026

Cite this article as: Oguz T., Aydın M.Ş., Kerman B.E. *et al.* Label-free holotomographic imaging of brain myelin. *Sci Rep* (2026). https://doi.org/10.1038/s41598-026-65156-6

Tuba Oguz, Mehmet Şerif Aydın, Bilal Ersen Kerman & M. Fatih Toy

Label-Free Holotomographic Imaging of Brain Myelin

Tuba Oguz[1,2], Mehmet Şerif Aydın[1], Bilal Ersen Kerman[3,1]*, M. Fatih Toy[4,5,6]*

[1]Regenerative and Restorative Medicine Research Center (REMER), Research Institute for Health Sciences and Technologies (SABITA), Istanbul Medipol University, Istanbul, Turkey

[2]Department of Neuroscience, Graduate School of Health Sciences, Istanbul Medipol University, Istanbul, Turkey

[3]Current Address: Department of Neurology, Keck School of Medicine, University of Southern California, Los Angeles, California, United States

[4]Biophotonics and Computational Imaging Laboratory (Phi-X), Biotechnology and Bioengineering Research Center, Research Institute for Health Sciences and Technologies (SABITA), Istanbul Medipol University, Istanbul, Turkey

[5]Department of Biomedical Engineering, School of Engineering and Natural Sciences, Istanbul Medipol University, Istanbul, Turkey

[6]Department of Electrical and Electronics Engineering, School of Engineering and Natural Sciences, Istanbul Medipol University, Istanbul, Turkey

* These authors are co-corresponding authors and are listed in no particular order. email addresses: kerman@usc.edu and mftoy@medipol.edu.tr

ABSTRACT

Quantitative assessment of myelin integrity is essential for understanding demyelinating diseases and evaluating remyelinating therapies. Transmission electron microscopy (TEM) is the gold-standard for *g*-ratio quantification but is slow, labour-intensive, and destructive. Here we introduce a rapid, label-free approach that combines holotomographic imaging with a point-spread-function-aware model to infer axon diameter, myelin sheath thickness and *g*-ratio in mouse corpus-callosum cryosections. Our system captures 100 distinct oblique illumination angle holograms in 45 s per field of view and reconstructs three-dimensional refractive-index maps at 335 nm lateral and 2.2 µm axial resolution. Concentric RI profiles were fitted with a model to extract axon diameter, sheath thickness and to estimate g-ratio values below the optical resolution limit. Specificity was tested in lysolecithin-induced demyelination and subsequent remyelination. From 160 axons in wild-type mice, holotomography yielded a mean estimated *g*-ratio of 0.736, closely matching TEM measurements of the same strain (0.721). Remyelination increased the estimated g-ratio to 0.740 versus 0.704 in contralateral control tissue, confirming detection of the thinner newly formed myelin. Holotomography therefore provides a cost-effective, high-throughput platform for quantitative myelin morphometry and screening of remyelinating compounds.

Keywords: Myelin, Label-free imaging, Refractive index, Holotomography, Remyelination, g-ratio

Introduction

Myelin is a unique multi-layered, lipid-rich structure that is crucial for neuronal survival, function, and electrical impulse propagation[1–4]. Several layers of specialized membrane

extensions of glial cells wrap around axons, and the compaction of these layers form myelin[4,5]. Oligodendrocytes in the central nervous system (CNS) and Schwann cells in the peripheral nervous system (PNS) are the glial cells responsible for myelin sheath production and maintenance throughout life[4,6]. Myelin acts as an insulation layer around axons, increasing electrical impulse conduction and supporting neuronal health[3,4,7,8]. Defects in myelin formation and maintenance, or disruptions in the myelin sheath, not only lead to slower electrical impulse conduction but also render axons vulnerable to immune cell attacks or metabolic defects, resulting in subsequent degeneration[6]. Consequently, myelin defects result in the occurrence of several disorders, such as multiple sclerosis (MS), Pelizaeus-Merzbacher disease (PMD), and Niemann-Pick disease (NPD)[9]. Although remyelination can occur, in many cases, achieving complete remyelination is extremely rare[10,11]. Moreover, the newly formed myelin is thinner[11,12].

Myelin imaging is an integral part of neuroscience research. Immunostaining is a well-established and widely used technique for visualizing myelin via the detection of proteins such as myelin basic protein (MBP), proteolipid protein (PLP), and myelin oligodendrocyte glycoprotein (MOG)[13–15]. Fluorophores or chromophores attached to protein-specific antibodies or secondary antibodies that recognize protein-specific antibodies allow visualization of myelinated axons and myelin-rich white matter structures in the CNS, such as the corpus callosum[14,15]. Immunostaining is a highly specific technique; however, its efficiency depends on several factors, such as fixation, sample thickness, permeabilization, and protein localization. Quantitative analysis of myelination by immunostaining is not always reliable in control and disease models since permeabilization or demyelination exposes hidden myelin proteins by disrupting the lipid-

rich myelin sheath[6]. Furthermore, the information provided by immunostaining is limited with the diffraction limit of optical microscopy systems, and finer details such as myelin thickness are not resolvable. Researchers overcome these limitations by transmission electron microscopy (TEM) imaging or label-free imaging.

TEM, with its nanometer-scale resolution, can serve superior myelin quantification and determination of myelin health compared to other methods[16]. It allows researchers to visualize the layered structure of the myelin sheath and accurately measure myelin thickness and axonal diameter. The g-ratio is a widely used parameter for assessing the myelination degree of axons, and is defined as the ratio of the axon diameter (d) to the diameter of the entire structure (myelin + axon, D), and shown as $g-\text{ratio} = d/D$[17,18]. TEM imaging of myelinated axons is the gold standard for calculating the g-ratio[19-22]. Despite its exceptional resolution and ability to provide detailed examination of the myelin sheath, TEM has limitations. This technique requires extensive preparation of the samples, and the equipment costs can be prohibitive[6,23]. While TEM enables detailed analysis of the myelin sheath, obtaining a global myelination assessment is time-consuming due to the low throughput imaging[24].

Over the last few years, several label-free imaging methods have been developed utilizing the unique physical properties of myelin[6,25-30]. Due to its lipid-rich content and multi-layered structure, myelin expresses highly organized refractive index distribution exploitable by the means of nonlinear optical effects (Coherent Anti-Stokes Raman Scattering – CARS; Third Harmonic Generation Microscopy – THG)[26-29,31] or spectral reflection behaviour (Spectral Confocal Reflectance Microscopy – SCoRe; Spectral Reflectometry – SPeRe)[6,25,30]. These methods offer advantages over immunostaining and

TEM, such as ease of use, simple or no sample preparation, and potential for live imaging, making them attractive for the quantitative analysis of myelin. CARS is based on the contrast created due to the vibrational frequency differences of CH_2 bonds in lipids, resulting in a greater signal from lipids that can be separated from axonal and extracellular space signals[32,33]. In THG microscopy, the interface between lipids and the aqueous extracellular space creates the THG signal[26]. g-ratio measurements have been reported for CARS and THG imaging of the rodent sciatic nerve, which provides an ideal imaging environment with sparsely distributed large myelinated axons[26,27]. However, in the corpus callosum the calculated g-ratio deviates significantly from TEM values[31] because the diffraction-limited point spread function (PSF) broadens the measured diameter of the entire structure (D), artificially lowering g-ratio. Imaging by SPeRe is based on the thin-film interference principle; the light scattered from myelin has different path lengths at different myelin thicknesses. Spectroscopic analysis of the reflected light allows nanoscale investigation of the degree of myelination, myelin and axonal swelling[30,34]. In SPeRe the axon diameter—and therefore the g-ratio—are not measured directly; they are inferred by matching each recorded reflectance spectrum to a pre-computed library of model spectra that assume fixed lamellar thicknesses and refractive-index values.

Another marker-free method, holotomography[35-41], creates volumetric refractive index (RI) maps of transparent specimens. In our previous holotomography study on cultured neurons[42], we noticed a distinctive double-peaked RI line-shape around myelinated neurites, although we did not yet label it formally. Here, we show that this feature is also present in the densely packed mouse corpus callosum and is absent from unmyelinated axons, establishing it as a myelin-specific signature for rapid, label-free identification.

Although the constituent lamellae are far below the optical resolution, their combined influence on the blurred RI profile is predictable. By extending the concentric-lamellae model used in spectral reflectometry (SCoRe/SPeRe) with an explicit PSF term, we derive a closed-form equation set that converts the effective RI profile directly into axon diameter, wrap number and g-ratio. Because RI is an intrinsic property, its measured values are independent of illumination power, exposure time or bleaching, unlike intensity-based imaging methods. We validate this approach in the mouse corpus callosum, show its specificity through a demyelination-remyelination model, and confirm its accuracy against gold-standard electron microscopy measurements. This work establishes holotomography as a powerful, high-throughput tool for the quantitative analysis of myelin, opening new avenues for better understanding demyelinating diseases.

Results

Axonal and myelin imaging via holotomography

The fundamental concept of holotomographic imaging and its utilization in myelin imaging are visualized in Figure 1. Holotomography relies on the volumetric synthesis of the sample scattering potential from a series of oblique-angle illumination digital holographic microscopy images[39] (Figure 1a). A tomographic RI distribution is numerically reconstructed (the details of the imaging system and reconstruction are provided in the Materials and Methods section and Supplementary Method 1.). Resolution of the resulting RI volume is ultimately confined by the diffraction limit of the synthesized 3D aperture[37],

yielding 335 nm lateral and 2.2 μm axial resolution for the imaging system. Hence, the image of any feature below these limits expresses a blur.

The process of myelination via wrapping and subsequent compaction results in a well-defined and strictly periodic layers of membrane (m), cytosolic proteins (c), membrane (m), and extracellular proteins and space (e) (Figure 1b). This periodic structure is terminated by a periaxonal space (p) before the membrane of the axon. Each of these components has a distinct thickness (t_m=5 nm, t_c=3 nm, t_e=5 nm, t_p=12 nm) and RI (n_m=1.5, n_c=1.47, n_e=n_p=1.35) that are well documented in the literature[30]. A unit of m, c, and m, separated by e, forms a myelin layer (ML) (Figure 1b). A representative RI profile of a 3-myelin layer wrapped axon is shown in Figure 1b with the title “Physical n values”.

Because each component’s thickness is far below the resolution limit, individual layers are not resolvable. However, an effective (averaged) RI profile after the PSF blurring is measured as illustrated in the same figure under the title “Measured n values”. Here, the refractive indices are shown for the same 3-layer wrapping scenario. This distinctive double-peaked profile serves as a myelin-specific signature that differentiates myelinated from unmyelinated axons, and crucially it is based on an intrinsic material property (RI) rather than emitted light intensity. In fluorescence, CARS or THG imaging the recorded signal scales with illumination power, exposure time, detector gain and photobleaching, so any PSF-induced smoothing changes the peak intensity in a way that cannot be calibrated back to structural information. By contrast, holotomography directly retrieves the complex optical field and converts it to absolute RI, which is independent of such acquisition parameters. The PSF lowers the measured peak n value in a predictable manner, enabling quantitative estimation of the unresolved structural information (see

Supplementary Method 2 and Supplementary Fig. 3 - 6 for PSF-convolution simulations). Owing to the well-defined thicknesses and refractive indices of myelin layer components, it is possible to estimate the number of myelin layers wrapped around an axon from the peak RI values. By using the estimated number of wrapping layers or the total thickness of the myelinated region, it is also possible to calculate the g-ratio. The results based on the estimation of the g-ratio are explored in the following sections.

Myelinated axons are detectable with 3D holotomographic imaging

The corpus callosum of the mouse brain was chosen for holotomographic imaging due to its compact and dense structure with several longitudinally extending myelinated axons. To determine the optimal sample thickness for visualizing myelin in our holotomographic imaging system, slices at different thicknesses ranging from 5 μm to 30 μm with 5 μm increments were imaged. The obtained images were inspected for the best longitudinal myelin appearance (Supplementary Fig. 1). The 5 μm thickness was selected as the optimal thickness and was therefore used for all subsequent analyses.

In the 100 μm × 100 μm field of view (FOV), the longitudinal appearance of myelin and axons was observable via our imaging system (Figure 1c). A single profile of high-low-high refractive indices formed one myelinated axon, where the blue arrowheads show the myelin sheath and the yellow arrowhead shows the axon (Figure 1d). In the RI volume, the YZ plane resolves the cross section of myelinated axons, where myelin appears as a myelin specific signature (blue arrowheads) (Figure 1e). Thus, in our imaging system, compact myelin around axons is distinguishable due to its different RI properties in the dense and crowded environment of the corpus callosum.

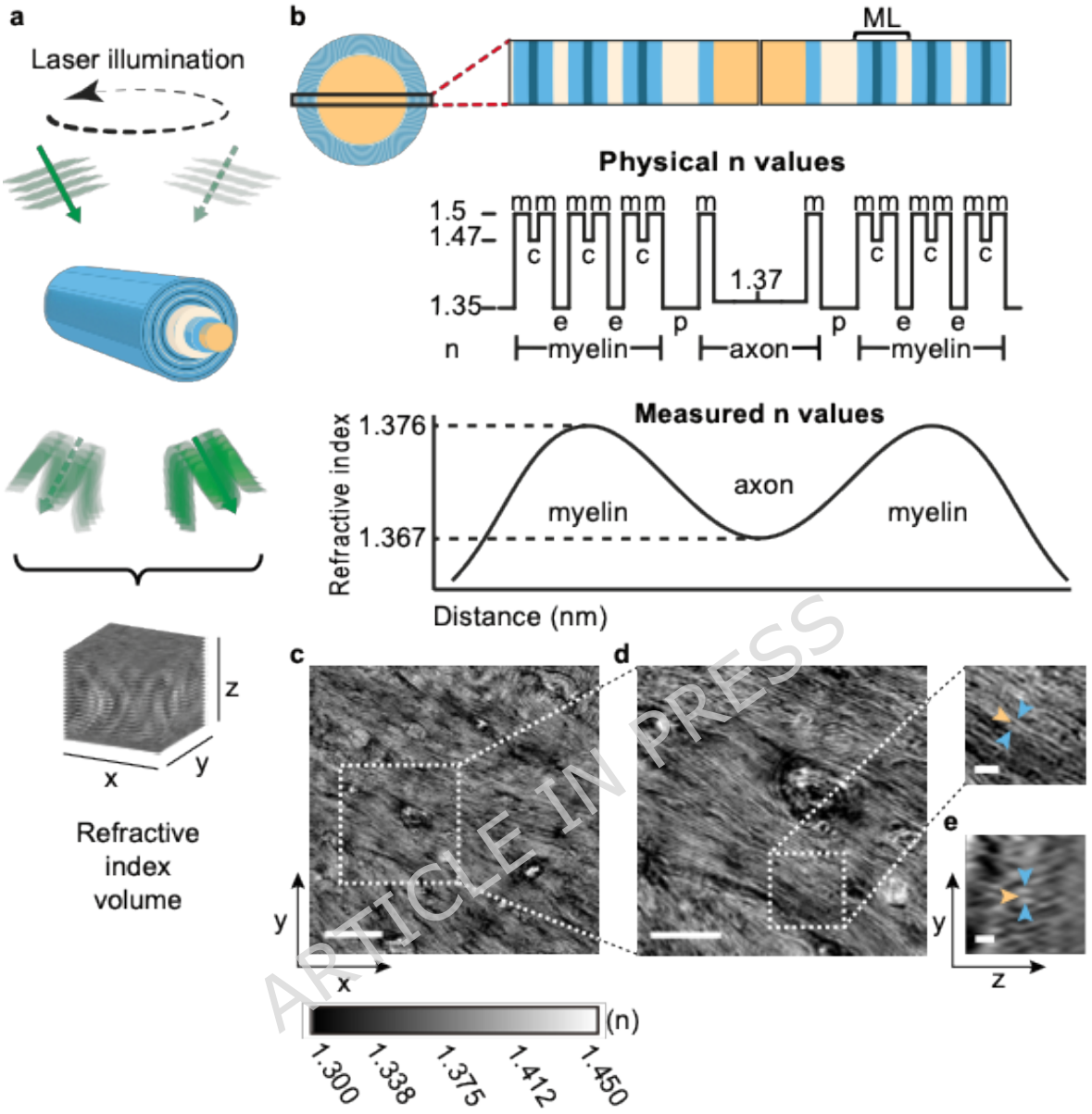

Figure 1: Holotomographic imaging methodology of myelin in the corpus callosum. **a** Working principle of holotomographic imaging. The green arrow shows one illumination direction, and the dashed arrow shows another illumination direction. **b** A representative schematic cross section of a myelinated axon. In the zoomed-in section next to it, three out of six layers of a scaled myelinated axon drawing are shown (ML=compacted myelin layer). A representative RI (n) profile of a myelinated axon (m=membrane, c=cytosolic

proteins, e=extracellular proteins and space, p=periaxonal space, and a=axon). Beneath that, a RI profile that is physically accessible by the imaging system (with a system of resolution 335 nm lateral, 2200 nm axial). Experimentally accessible myelin specific signature has a characteristic double-peaked profile. **c-d** Longitudinal appearance of myelinated axons. **c** A representative holotomographic image of 5 μm thick tissue sections from the corpus callosum region (scale bar: 20 μm). **d** Zoomed-in images clearly showing myelin specific signatures. The blue and yellow arrowheads correspond to the peaks and trough in the “measured n values”, respectively (scale bars: 10 μm and 2 μm). **e** In the YZ plane, a myelin specific signature (blue arrowheads) surrounding the axon (yellow arrowhead) is visible (scale bar: 1 μm). Colorbar indicates the relevant refractive index (n) values.

3D holotomographic imaging of the CNS demyelination model

To exclude the possibility of the double peaked RI profile, myelin specific signature, reflecting the ordered axons rather than myelin, we evaluated our imaging system on the demyelinated corpus callosum. Demyelination is the disruption of the ordered structure of lipid-rich myelin membranes. Lysolecithin (L-α-Lysophosphatidylcholine; LPC) is widely used to create chemically induced CNS demyelination models[43]. To induce demyelination, LPC was injected into the corpus callosum of Prism JD1989 mouse (Figure 2a-b). In Prism JD1989 mouse, myelin in the corpus callosum is easily distinguishable via intense cerulean fluorescent protein (CFP) labelling of oligodendrocytes. LPC-induced demyelination was observable via a decrease in the CFP signal in the corpus callosum (Figure 2b; dashed region). When the same demyelinated region was investigated by holotomographic imaging, the myelin specific signature was

lost (Figure 2c). The signature was clearly visible in the non-lesioned region (Figure 2d). Therefore, myelin specific signatures were due to the presence of myelin in the region of interest.

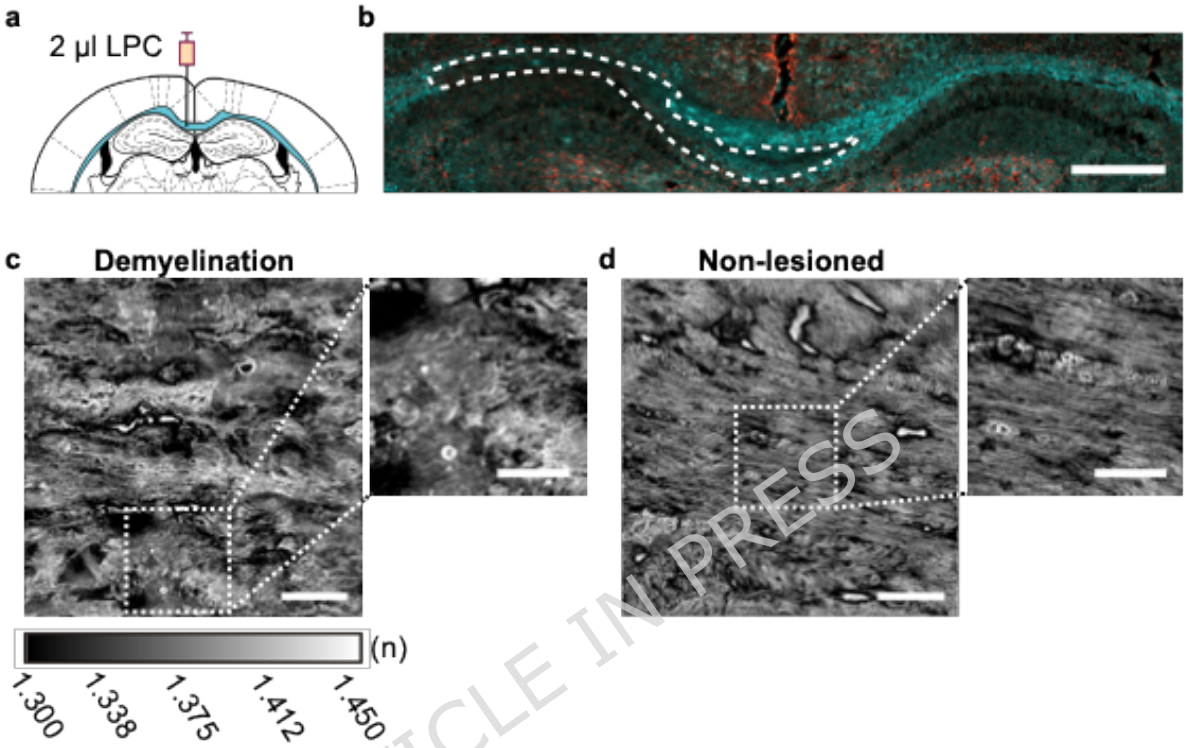

Figure 2: Loss of the myelin specific signature after LPC induced demyelination. **a** Injection of 2 µL LPC into the corpus callosum of a Prism JD1989 mouse; imaging performed at 3 days post lesion (dpl). **b** Widefield fluorescence: oligodendrocytes expressing cerulean fluorescent protein (CFP, cyan) delineate myelin; astrocytes express DsRed-Max (red). The dashed outline marks the lesion (scale bar, 500 µm). **c** Holotomographic refractive-index image from the LPC lesion showing absence of the characteristic double-peaked myelin signature (scale bars: 20 µm and 10 µm). **d** Contralateral non-lesioned corpus callosum showing preserved myelin-specific signature. (scale bars: 20 µm and 10 µm). Colorbar indicates the relevant refractive index (n) values.

A quantitative metric of the degree of myelination

The *g*-ratio—defined as the ratio of axon diameter (d) to fiber diameter (D = axon + myelin)—is a dimensionless index of myelination[11,17]. Because holotomography yields absolute refractive-index profiles, we asked whether sub-diffraction myelin thickness could be estimated from those profiles and used to compute *g*-ratio.

The RI profiles of myelinated axons were analysed in MATLAB (Figure 3a). As expected, the experimental traces resembled the PSF-blurred theoretical profiles (compare Figures 1b and 3a). We extracted the full width at half maximum (W_f, µm) and the peak separation (w_p, µm) between the two maxima (n_{max1} and n_{max2}) and used these to estimate the fibre diameter D_e (Equations 1–5). Peak heights, together with fixed lamellar refractive indices and thicknesses (Materials and Methods section and Supplementary Method 2), provided the number of wraps, from which we obtained estimated myelin thickness and axon diameter d_e. The estimated *g*-ratio (*g*$_e$-ratio) was then computed as d_e/D_e . (Equations 4–5). Profiles were included only if the minimum between two maxima (n_{min} in Figure 3a) is above the background RI. Myelin thickness estimates reported here are derived as $t_{myelin} = D_e - d_e$ from the same diameter estimates used to compute *g*$_e$-ratio, and are therefore internally consistent with the *g*-ratio readout.

From 160 axons pooled across multiple fields of view we obtained a median *g*$_e$-ratio of 0.745 and a mean ± SD of 0.736 ± 0.112 (Figure 3b). Our mean *g*$_e$-ratio is statistically not different from the *g*-ratio calculated from EM images of the same strain of mice, 0.721±0.06 (n=133; p=0.18; Supplementary Fig. 15). These values also fall within published *g*-ratio range of the corpus callosum from EM measurements, (0.72–

0.81)[17,44,45]. Thus, holotomographic RI profiling provides a high-throughput complement to TEM for estimating *g*-ratio distributions across large axon populations.

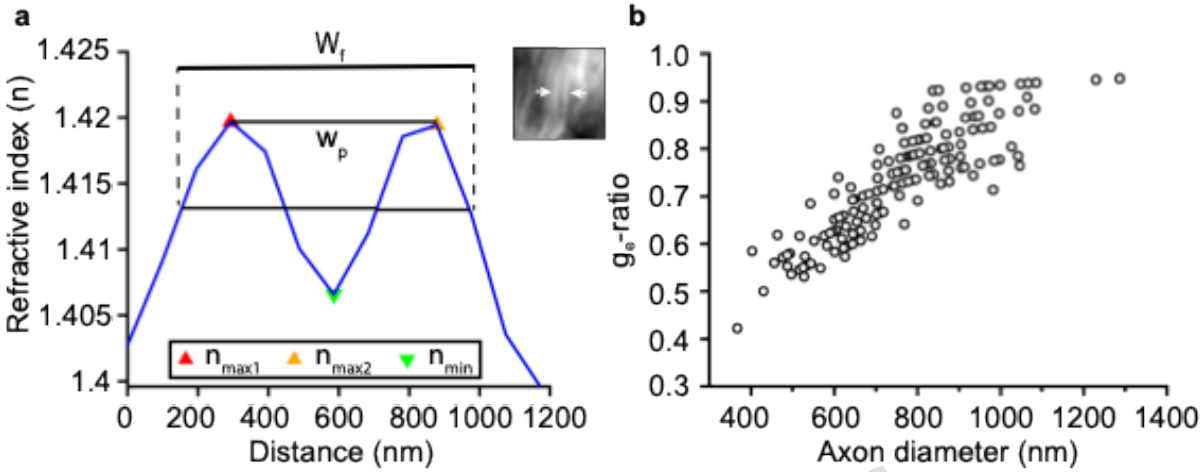

Figure 3: Estimating the g-ratio from holotomographic RI profiles. **a** Experimental RI profile of the myelinated axon from the holotomographic image at the inset. W_f is the distance at the FWHM relative to n_{max1}, n_{max2}, and n_{min}. w_p is the distance between the two maxima. W_f, w_p, n_{max1}, and n_{max2} were used in the calculation of the g_e-ratio. The n_{max1} and n_{max2} values are dependent on the myelination level of the axon. **b** Scatter plot of the g_e-ratio vs. axon diameter from the corpus callosum (n=160). The mean±SD g_e-ratio was 0.736±0.112, and the median g_e-ratio was 0.745.

Recovery of the myelin specific signature in remyelination

Remyelination is the recovery of the demyelinated region, and in general, the newly generated myelin sheaths are thinner even after complete recovery (i.e., higher *g*-ratio)[11,12]. In the LPC-induced demyelination model, recovery starts around 5-7 dpl[46] and is completed by 21 dpl[43,47]. To evaluate the sensitivity of our g_e-ratio calculation method from holotomographic images, we imaged the recovered corpus callosum region at 21

dpl. Holotomographic imaging revealed that the differing refractive indices and myelin specific signatures were qualitatively detectable (Figure 4a). Significantly, g_e-ratios of remyelinated axons (n=91) were higher than the control axons on the contralateral side of the same mouse (n=93; mean±SD 0.740±0.11 and 0.704±0.111 respectively; p=0.0270; Figure 4b). A scatter plot of the g_e-ratios and a floating bar graph of myelin thickness showed that the newly generated myelin was thinner than the control across the various axonal diameters (Figure 4c and d). In conclusion, we detected differences between primary and reformed myelin proving that g_e-ratio calculation using holotomographic imaging was a viable method for analysis of CNS demyelination and remyelination.

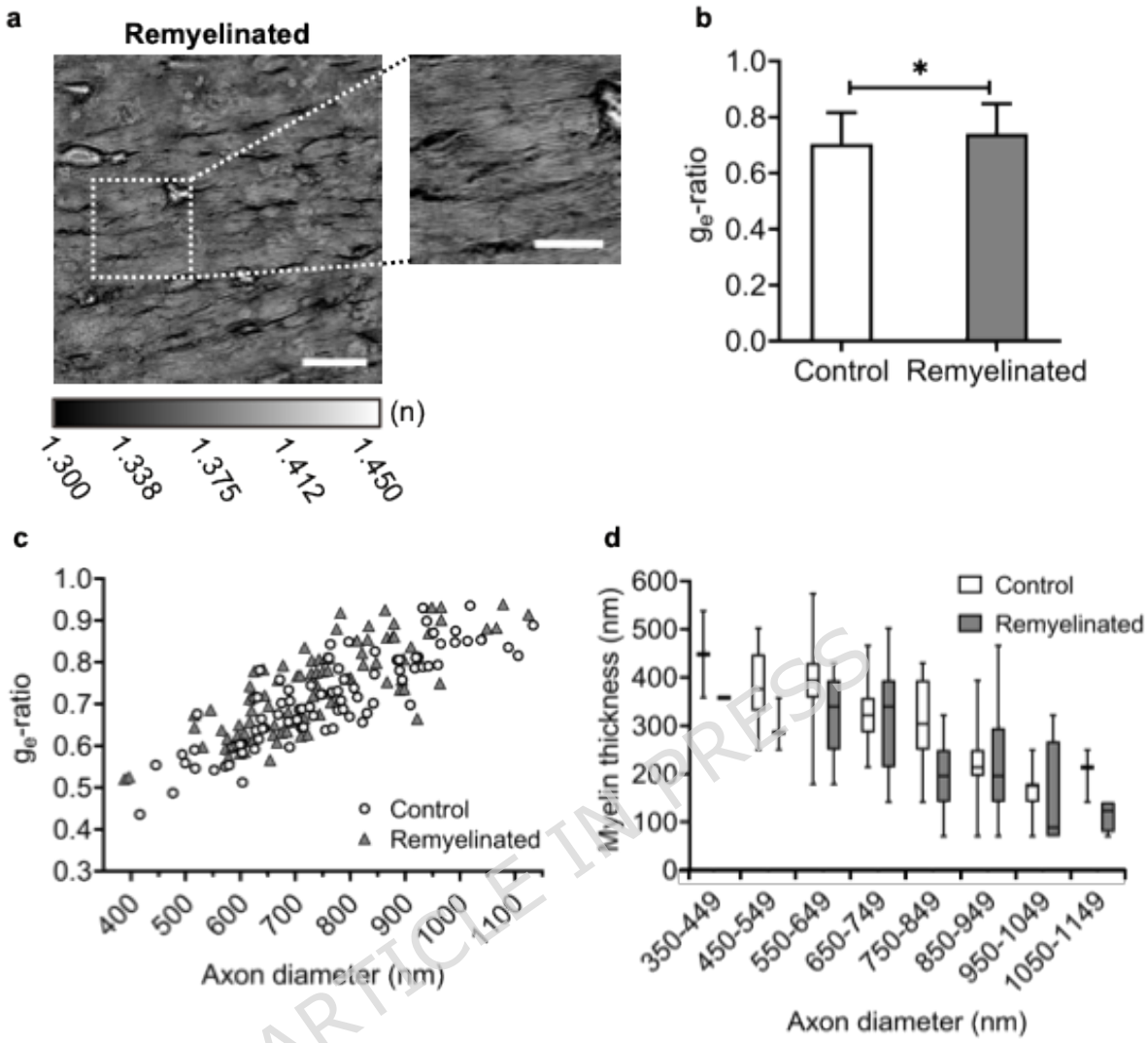

Figure 4: Remyelination restores the myelin-specific RI signature and increases the estimated g_e-ratio. **a** Holotomographic RI image at 21 dpl show re-emergence of the characteristic double peaked myelin signature in the lesion site. Scale bars: 20 µm (main), 10 µm (inset). **b** g_e-ratio for remyelinated axons is higher than for contralateral non-lesioned controls, indicating thinner sheaths (mean ± SD: control = 0.704 ± 0.111, n = 91; remyelinated = 0.740 ± 0.110, n = 93). Points pool per-axon values across multiple fields of view. **c** Scatter plot of the control and remyelinated axon g_e-ratio vs axon diameter shows higher g_e-ratios for remyelinated axons. **d** Estimated myelin thickness vs axon

diameter graph demonstrates thinner myelin in the remyelinated groups in a pattern similar to that of the control group. (Control, n=91; Remyelinated, n=93) Colorbar indicates the relevant refractive index (n) values

Discussion

Due to its biological significance and distinct properties, myelin imaging has been at the forefront of microscopic imaging advancements[6,25-27,29,30,42]. Here we applied three dimensional holotomography to analyse label-free myelin in ex vivo mouse brain. Our work has two main contributions. First, we identify a characteristic double-peaked refractive-index profile that appears only around compactly myelinated axons, the “myelin specific signature”. Second, by combining a concentric lamellae model with an explicit PSF term, we derive a closed form estimator that recovers axon diameter, myelin thickness and the g_e-ratio from the blurred RI profile (Equations 1–5). Taking advantage of the known lamellar refractive indices and thicknesses[30], we estimate wrap number and consequently the total thickness of the myelin sheath and the g_e-ratio.

A myelinated axon is composed of the axon cytoplasm and its membrane surrounded by glial membranes[4,5]. The membranes are cholesterol-rich and tightly apposed, leaving negligible cytoplasm between the two layers[48,49]. The extracellular space between layers is almost non-existent (Figure 1)[30]. This architecture both provides strong optical contrast and constrains modelling assumptions, and has motivated multiple label-free approaches to myelin[6,25-27,29,42,50].

Animal models of demyelination are useful tools for investigating demyelinating lesions and recovery processes, and for testing reagents/drugs to accelerate remyelination[51].

LPC is the reagent of choice for creating a chemically induced focal demyelination model due to the well-defined time course of demyelination and subsequent remyelination[51]. Consistent with the expected time-course of the LPC model, holotomography showed loss of the myelin-specific signature in lesions and its re-emergence during remyelination, supporting the specificity of the signature for compact myelin. Quantitatively, the estimated g_e-ratio increased in remyelinated axons relative to contralateral controls, indicating thinner sheaths, in agreement with TEM benchmarks and prior corpus-callosum ranges.

The g-ratio remains a central index of myelination. TEM is the gold standard but requires specialised sample preparation and is low-throughput[18-22,24]. Nonlinear-optical methods have reported g-ratios in peripheral nerves[26,27], but values in densely packed CNS tracts can deviate from TEM[31]—likely reflecting optical resolution limit. Our holotomographic estimates agreed with paired TEM measurements in the same strain and with the literature[17,44,45,52,53,54], supporting holotomography as a high-throughput complement to TEM for *g*-ratio distributions.

Holotomographic imaging provides a comparatively rapid workflow for quantitative myelin analysis when compared with conventional TEM (Supplementary Table 1). Following fixation and cryoprotection, sample preparation for holotomography mainly involves embedding, cryosectioning, and mounting of tissue sections, which can be completed within several hours, whereas TEM requires multi-day preparation including heavy-metal staining, resin embedding, and ultramicrotomy (see supplementary Materials and Methods).

Image acquisition is also relatively rapid, as a 100 μm × 100 μm three-dimensional refractive index volume can be acquired in approximately 45 seconds, enabling imaging of multiple regions within a short time. Although computational reconstruction and analysis are required, these steps can be performed using automated batch processing. Consequently, the total workflow time after fixation is substantially shorter than that required for EM-based morphometric analysis, supporting the use of holotomography as a relatively high-throughput approach for three-dimensional myelin imaging.

In conclusion, holotomographic RI profiling combines a qualitative myelin-specific signature with a PSF-aware quantitative model to estimate axon diameter, myelin thickness and *g*-ratio in ex vivo mouse corpus callosum. The approach detects demyelination and its repair and provides a practical, scalable read-out for studies of myelin biology and for screening candidate remyelinating interventions relevant to MS, PMD and NPD.

The present implementation targets ex vivo cryosections and therefore complements—rather than replaces—either EM or in vivo imaging. Compared with TEM, holotomography trades nanoscale ultrastructural resolution for faster volumetric sampling over larger tissue areas, while remaining label-free. Compared with intensity-based label-free contrasts (e.g., CARS/THG), holotomography retrieves absolute refractive index (RI) rather than emitted intensity, and our PSF-aware model enables estimation of g-ratio and related parameters from the characteristic RI signature of compact myelin. Optical penetration and motion currently limit deep-brain in vivo use; accordingly, the principal applications are high-coverage morphometry in histology workflows and preclinical demyelination/remyelination models.

MRI-based g-ratio mapping aims to estimate an aggregate g-ratio in vivo by combining myelin-sensitive and axon-sensitive MRI measures within a modelling framework[55]. However, MRI *g*-ratio remains model-dependent and subject to known confounds[56,57]. In this context, holotomographic RI profiling can provide a practical intermediate-scale reference between EM and MRI, supporting calibration/validation studies and scalable screening of candidate remyelinating interventions under consistent tissue preparation.

The present study benchmarks the estimated *g*-ratio against EM but does not include a direct, axon-by-axon validation of absolute myelin thickness against EM. Because thickness in our pipeline is derived from the same estimated diameters, agreement in *g*-ratio supports internal consistency of the diameter estimates; however, absolute thickness values should be interpreted cautiously and as specific to the present preparation and calibration. Fixation can induce tissue and cellular shrinkage and may alter RI in a protocol- and compartment-dependent manner[58-60]. Because *g*-ratio is a ratio of diameters, it is expected to be less sensitive to uniform shrinkage than absolute thickness, and one neuropathology study reported no significant change in *g*-ratio across processing conditions within their dataset[58]. Reported fixation-induced RI changes are mixed—e.g., increased RI reported for peripheral myelin[61] and decreased cytoplasmic RI reported in holotomographic single-cell analyses[59]—so we interpret absolute RI and thickness values as protocol-specific, while emphasizing that comparative *g*-ratio trends should remain robust under consistent preparation.

Despite these limitations, holotomographic RI profiling provides a label-free and scalable route to quantify axon diameter, myelin thickness and *g*-ratio from dense CNS white matter, while retaining the ability to visualize a characteristic myelin-specific signature. In

demyelination and remyelination, the approach offers a practical way to survey large axon populations and detect subtle shifts in myelin morphology under a consistent preparation protocol. With future co-registered EM validation and expanded automation of profile extraction, this framework could become a useful intermediate-scale bridge between ultrastructural EM studies and larger-scale imaging modalities, supporting both mechanistic myelin biology and preclinical screening of remyelinating interventions.

Materials and Methods

Animals

All surgical and experimental procedures were approved by the Istanbul Medipol University Experimental Animal Care and Research Ethics Committee (IMU-HADYEK) in accordance with the European Economic Community Council Directive 86/609. Four wild-type (WT) BALB/c mice (Jackson ID: 000651) and one FVB-Tg(Prism)1989Htz/J (Jackson ID: 018068, Prism JD1989) mouse (male, 2 month-old) were used. All animals were obtained from The Jackson Laboratory, Bar Harbour, ME, USA; bred and maintained in the Istanbul Medipol University Animal Facility (MEDITAM). Two of the four WT animals were used to optimise tissue slice thickness. Animals with corpus callosum damage were excluded. In the prism JD1989 mouse, oligodendrocytes (cerulean florescent protein, CFP), astrocytes (DsRedMax), and neurons (yellow fluorescent protein, YFP; nuclear expression) express distinct fluorescent proteins[62]. All animals had ad libitum access to food and water, were exposed to a 12 hours/12 hours (h) light/dark cycle and were housed in 20–24 °C, and 40–60% humidity.

Demyelination and remyelination process

L-α-Lysophosphatidylcholine from bovine brain (lysolecithin; LPC; L1381, Sigma-Aldrich) was resuspended inresuspended in 0.9% NaCl to obtain a 2% stock solution and stored at -20 °C. Working aliquots of 1% LPC were prepared on the day of surgery. Anesthetized mice (ketamine 100 µg/g and xylazine 10 µg/g) were placed in a stereotactic instrument (David Kopf Instruments, Tujunga, CA, USA). Two microliters (2 µl) of 1% LPC in 0.9% NaCl was unilaterally injected intracranially with a flow rate of 120 nl/min set by a micromanipulator (Narishige, East Meadow, NY, USA) to the corpus callosum (coordinates: 0.3 mm lateral, -1.7 mm rostral to bregma, 1.7 mm deep to the brain surface including the skull thickness) according to the Mouse Brain Atlas[63]. The injection pipette was kept in place for 10 minutes (min) for LPC to diffuse and prevent liquid reflux and was withdrawn slowly.

Mice were sacrificed at 3 dpl to visualize demyelination. For remyelination, mouse received standard postoperative care for 21 dpl and then was sacrificed. The contralateral hemisphere of the lesion site was used as control. One prism mouse was subjected to demyelination and one WT mouse was subjected to remyelination. During post operative care, the animals had ad libitum access to food and water, were exposed to 12 h/12 h light/dark cycle and were housed in 20–24 °C, and 40–60% humidity.

Sample preparation for imaging

Mice were anesthetized (ketamine 100 µg/g and xylazine 10 µg/g) and sacrificed by transcardial perfusion with 1x buffered phosphate saline (1xPBS) at 4 °C, followed by 4% paraformaldehyde (PFA) at 4 °C for fixation. The brains were removed and postfixed for 24 h in 4% PFA before switching to 30% sucrose solution for cryoprotection.

Brain slices' holotomographic imaging and direct imaging were obtained from the same brain as serial brain slices for all experimental conditions. Briefly, brains were embedded in optimal cutting temperature medium (OCT, Tissue-Tek), and coronal slices at different tissue thicknesses (5, 10, 15, 20, 25, and 30 μm) were collected using a cryostat device. Slices were mounted between No. 1.5H coverslips (170 ± 5 μm; 0107222, Marienfeld Superior, Germany) using 0.09 mm double-sided tape as a spacer. Fluoromount (F4680, Sigma-Aldrich) with the refractive index (RI) of 1.354 was used for mounting.

Confocal imaging

Images of the brain slices of Prism JD1989 mouse were acquired on a Zeiss LSM780 laser scanning confocal microscope with a 20x objective. The images were taken as several tiles and z-stacks; final images were obtained after stitching and maximum intensity projection. Images were processed on Zen Software (Zeiss) and Fiji[64].

Holotomographic imaging and optimization

A custom off-axis Mach-Zehnder interferometric microscope with a motorized gimbal mirror (OMG-T4A, Zaber, Canada) was employed for holotomographic imaging[42] (Supplementary Fig. 2). Coherent green laser light (λ = 520 nm) was split into reference and object arms. A motorized gimbal mirror on the object arm was conjugated to the sample plane through two 4-f imaging systems. A high-numerical-aperture microscope objective (CFI Plan Fluor 60x, 0.85 NA; Nikon Instruments Inc., USA), as the last element of the 4-f systems assures illumination angle scan on a cone with a large apex angle. The sample scattering was collected by another microscope objective with identical properties (CFI Plan Fluor 60x, 0.85 NA; Nikon Instruments Inc., USA) and imaged on a CMOS

camera (UI-3060CP-M-GL, IDS Imaging, Germany) after passing through a tube lens (f = 200 mm, ITL200; Thorlabs Inc.). For each tomographic acquisition, 100 off-axis holographic images of a sample were acquired from different illumination directions within 45 seconds. From each off-axis hologram, a 2D complex field was retrieved[65,66]. The retrieved scattering fields were synthesized in the 3D Fourier space to reconstruct the 3D refractive index distribution through the Rytov Approximation[38]. After reconstruction and remapping, RI volumes were inspected and analysed without additional spatial denoising or intensity normalisation. Quantitative feature extraction was performed on the reconstructed RI volumes as described below.

Quantitative analysis, and g_e-ratio calculation

For the quantitative analysis of the myelin-axon-myelin profiles in each holotomographic image, refractive index vs distance plots were extracted using Fiji software[64]. A single RI line profile for g_e-ratio estimation was extracted perpendicular to the fibre axis (across the myelin–axon–myelin cross-section) from the reconstructed 3D RI volume (e.g., YZ plane in Figure 1e) where the double-peaked myelin signature was most clearly resolved. The distance (W_f) at full width at half maximum (FWHM) and the distance (w_p) between n_{max1} and n_{max2} were calculated on MATLAB with a self-written script. Maximum refractive indices (n_{max1}, n_{max2}), W_f and w_p values were used in the g_e-ratio calculation (Figure 3a, Equations 1-5). RI profiles were extracted from the reconstructed volumes using identical sampling geometry across conditions. Profiles were included only when a clear double-peaked signature was present, with a local trough n_{min} between the two maxima that remained above the local background RI.

Using fixed lamellar parameters from Kwon *et al.*[30] and our system's PSF, we derived a piecewise estimator (Equations 1-5; Supplementary Method 2) that returns the estimated outer diameter of the myelinated axon D_e and axon diameter d_e of the well-known $g-\text{ratio} = d/D$ formula, respectively. The average of the maximum refractive indices ($\grave{n}_{max}$) was used for the calculation of criterion (c), which represents the estimated myelin thickness (t_{myelin}) relative to average $\grave{n}_{max}$ (Equations 1-3). α and β are empirically determined, PSF dependent parameters. γ and ζ are the constants defining thickness increment per wrapping based on Kwon et al.'s model (α = 209.5, β = 286.7, γ = 36, and ζ = 34; Supplementary Method 2).

The intermediate variable c ("criterion") denotes the number of compact wrapping cycles in the concentric-lamellae model. Under the adopted lamellar geometry, each additional cycle contributes a constant thickness increment, hence $t_{myelin} = \gamma c + \zeta$, where $\gamma = 36$ nm is the thickness increment per cycle and $\zeta = 34$ nm is an offset term capturing the inner boundary thickness between the axon and the first compact layer. Because PSF blurring compresses peak RI values, the mapping from the experimentally accessible mean peak RI $\grave{n}_{max} = (n_{max\,1} + n_{max\,2})/2$ to c is instrument dependent. We therefore generate PSF-aware simulated profiles with known cycle counts c, extract $\grave{n}_{max}$, and fit $c = \alpha\grave{n}_{max} - \beta$; for our system $\alpha = 209.5$ and $\beta = 286.7$ (Supplementary Method 2; $R^2 = 0.979$, RMSE $= 0.834$ cycles). For large wrap counts, $\grave{n}_{max}$ becomes less sensitive (peak compression), and we therefore apply a piecewise estimator with a threshold at $c = 18$; the diameter-offset constants in Eqs. (4–5) (235 nm and 275 nm) are PSF-dependent offset terms obtained from the simulation library (Supplementary Method 2).

$$\grave{n}_{max} = (n_{max\,1} + n_{max\,2})/2 \quad (1)$$

$$c = \alpha \cdot \grave{n}_{max} - \beta \quad (2)$$

$$t_{myelin} = \gamma \cdot c + \zeta \quad (3)$$

$$g_e - ratio = d_e / D_e \begin{cases} D_e = 2W_f - w_p \; and \; d_e = D_e - t_{myelin} & for \; c < 18 \quad (4) \\ D_e = W_f + 275 \; and \; d_e = w_p - 235 & for \; c \geq 18 \quad (5) \end{cases}$$

The calibration procedure and residual analysis for α,β and the diameter-offset terms are provided in Supplementary Method 2 and Supplementary Fig. 7.

For the verification of our g_e-ratio calculation method, 160 profiles out of 164 profiles were included from WT mouse corpus callosum (Figure 3). To calculate the g_e-ratio to show remyelination, 93 profiles out of 94 profiles from remyelination, and all the 91 profiles from control were included in the study. For an axon to be counted as myelinated, there should be at least one myelin layer surrounding the axon. As criterion representing the myelin layers, data points with criterion<1 were excluded from the study (n=4 for Figure 3; n=1 from the remyelination group and n=0 from the control group for Figure 4). Sample sizes were determined in line with the published literature on *g*-ratio calculations. All experimenters were aware of the different sample type during image acquisition. Image processing and g_e-ratio calculations were done by a blinded researcher. 2 FOVs from each condition were analysed for g_e-ratio calculations.

Statistics

Statistical analyses were performed using GraphPad Prism 8 software (GraphPad Software Inc., La Jolla, California). Data were analysed using two-tailed unpaired Student's t-test, and $p<0.05$ was considered as statistically significant. Data assumed to be normally distributed.

Data availability

The authors declare that the data supporting the findings of this study are available within the paper and its supplementary information files. Any other information is available from the corresponding authors upon reasonable request.

Code availability

Custom MATLAB scripts and Fiji macros used for image acquisition, post-processing, data acquisition and analyses are available from the corresponding authors upon reasonable request.

Acknowledgments

We thank Gürkan Öztürk for his helpful discussions, and MEDITAM facility for the animal care.

Funding

This project was supported by the Scientific and Technological Research Council of Turkey (TUBITAK) under grants 116F437 (M.F.T.) and 120S327 (B.E.K.). T.O. was supported by the TUBITAK BIDEB 2211C. M.F.T. and B.E.K. were supported by the Turkish Academy of Sciences-GEBIP.

Author Contributions

T.O., M.F.T. and B.E.K. designed the experiments, interpreted the results, and wrote the manuscript. T.O. performed the animal experiments and sample preparation. M.Ş.A. performed electron microscopy. T.O. and M.F.T. performed the imaging, wrote the MATLAB codes and Fiji macros, and analysed the data.

Additional Information

Competing Interests: T.O., M.Ş.A. and B.E.K. declare no competing interests. M. F. T. is a co-founder and shareholder of Nanolive SA, a company that commercializes holotomography, no Nanolive products or revenue supported this study.

Materials & Correspondence: mftoy@medipol.edu.tr or kerman@usc.edu

References

1. Hartline, D. K. & Colman, D. R. Rapid conduction and the evolution of giant axons and myelinated fibers. *Curr Biol* **17**, R29–R35 (2007).

2. Jarjour, A. A. *et al.* The formation of paranodal spirals at the ends of CNS myelin sheaths requires the planar polarity protein Vangl2. *Glia* **68**, 1840–1858 (2020).

3. Fünfschilling, U. *et al.* Glycolytic oligodendrocytes maintain myelin and long-term axonal integrity. *Nature* **485**, 517–521 (2012).

4. Nave, K.-A. & Werner, H. B. Myelination of the nervous system: mechanisms and functions. *Annu Rev Cell Dev Bi* **30**, 503–533 (2014).

5. Karim, S. A. *et al.* PLP/DM20 expression and turnover in a transgenic mouse model of Pelizaeus-Merzbacher disease. *Glia* **58**, 1727–38 (2010).

6. Gonsalvez, D. G. *et al.* Imaging and quantification of myelin integrity after injury with spectral confocal reflectance microscopy. *Front Mol Neurosci* **12**, 275 (2019).

7. Philips, T. & Rothstein, J. D. Oligodendroglia: metabolic supporters of neurons. *J Clin Invest* **127**, 3271–3280 (2017).

8. Huxley, A. F. & Stämpeli, R. Evidence for saltatory conduction in peripheral myelinated nerve fibres. *J Physiology* **108**, 315–339 (1949).

9. Aydinli, F. İ., Çelik, E., Vatandaşlar, B. K. & Kerman, B. E. Myelin disorders and stem cells: as therapies and models. *Turk J Biol* **40**, 1068–1080 (2016).

10. Chari, D. M. Remyelination in multiple sclerosis. *Int. Rev. Neurobiol.* **79**, 589–620 (2007).

11. Franklin, R. J. M. & ffrench-Constant, C. Remyelination in the CNS: from biology to therapy. *Nat Rev Neurosci* **9**, 839–855 (2008).

12. Duncan, I. D., Marik, R. L., Broman, A. T. & Heidari, M. Thin myelin sheaths as the hallmark of remyelination persist over time and preserve axon function. *Proc National Acad Sci* **114**, E9685–E9691 (2017).

13. Winterstein, C., Trotter, J. & Krämer-Albers, E.-M. Distinct endocytic recycling of myelin proteins promotes oligodendroglial membrane remodeling. *J Cell Sci* **121**, 834–842 (2008).

14. Crawford, D. K., Mangiardi, M. & Tiwari-Woodruff, S. K. Assaying the functional effects of demyelination and remyelination: Revisiting field potential recordings. *J Neurosci Meth* **182**, 25–33 (2009).

15. Dai, J., Bercury, K. K., Ahrendsen, J. T. & Macklin, W. B. Olig1 function is required for oligodendrocyte differentiation in the mouse brain. *J Neurosci* **35**, 4386–4402 (2015).

16. Gibson, E. M. *et al.* Neuronal activity promotes oligodendrogenesis and adaptive myelination in the mammalian brain. *Science* **344**, 1252304 (2014).

17. Chomiak, T. & Hu, B. What is the optimal value of the g-ratio for myelinated fibers in the rat CNS? A theoretical approach. *Plos One* **4**, e7754 (2009).

18. Stassart, R. M., Möbius, W., Nave, K.-A. & Edgar, J. M. The axon-myelin unit in development and degenerative disease. *Front Neurosci-switz* 12, 467 (2018).

19. Gow, A. Myelin *g* Ratios: The Model Is in the Details. ASN Neuro 18(1), 2612034 (2026).

20. Oost, W., Meilof, J. F. & Baron, W. Multiple sclerosis: what have we learned and can we still learn from electron microscopy. Cell. Mol. Life Sci. 82, 172 (2025).

21. Craig, G. A., Ryan, L., Thapar, J., McNamara, N. B., Hoffmann, A., Page, D., Rose, J., Cox, S. R. & Miron, V. E. Reflective imaging of myelin integrity in the human and mouse central nervous systems. Front. Cell. Neurosci. 18, 1408182 (2024).

22. van der Weijden, C. W. J., Biondetti, E., Gutmann, I. W., Dijkstra, H., McKerchar, R., de Paula Faria, D., de Vries, E. F. J., Meilof, J. F., Dierckx, R. A. J. O., Prevost, V. H., Rauscher, A. & Quantitative myelin imaging with MRI and PET: an overview of techniques and their validation status. Brain 146(4), 1243–1266 (2023).

23. Skripuletz, T., Gudi, V., Hackstette, D. & Stangel, M. De- and remyelination in the CNS white and grey matter induced by cuprizone: the old, the new, and the unexpected. *Histol Histopathol* **26**, 1585–97 (2011).

24. Lee, A. J. *et al.* Volumetric refractive index measurement and quantitative density analysis of mouse brain tissue with sub-micrometer spatial resolution. *Adv. Photonics Res.* (2023) doi:10.1002/adpr.202300112.

25. Schain, A. J., Hill, R. A. & Grutzendler, J. Label-free in vivo imaging of myelinated axons in health and disease with spectral confocal reflectance microscopy. *Nat Med* **20**, 443–449 (2014).

26. Hajjar, H. *et al.* Label-free non-linear microscopy to measure myelin outcome in a rodent model of Charcot-Marie-Tooth diseases. *J Biophotonics* **11**, e201800186 (2018).

27. Lim, H. *et al.* Label-free imaging of Schwann cell myelination by third harmonic generation microscopy. *Proc National Acad Sci* **111**, 18025–18030 (2014).

28. Fu, Y., Huff, T. B., Wang, H.-W., Cheng, J.-X. & Wang, H. Ex vivo and in vivo imaging of myelin fibers in mouse brain by coherent anti-Stokes Raman scattering microscopy. *Opt Express* **16**, 19396 (2008).

29. Witte, S. *et al.* Label-free live brain imaging and targeted patching with third-harmonic generation microscopy. *Proc National Acad Sci* **108**, 5970–5975 (2011).

30. Kwon, J. *et al.* Label-free nanoscale optical metrology on myelinated axons in vivo. *Nat Commun* **8**, 1832 (2017).

31. Ozsvár, A. *et al.* Quantitative analysis of lipid debris accumulation caused by cuprizone induced myelin degradation in different CNS areas. *Brain Res. Bull.* **137**, 277–284 (2018).

32. Pallen, S., Shetty, Y., Das, S., Vaz, J. M. & Mazumder, N. Advances in nonlinear optical microscopy techniques for in vivo and in vitro neuroimaging. *Biophysical Rev* **13**, 1199–1217 (2021).

33. Farrar, M. J., Wise, F. W., Fetcho, J. R. & Schaffer, C. B. In vivo imaging of myelin in the vertebrate central nervous system using third harmonic generation microscopy. *Biophys J* **100**, 1362–1371 (2011).

34. Kwon, J., Lee, S., Jo, Y. & Choi, M. All-optical observation on activity-dependent nanoscale dynamics of myelinated axons. *Neurophotonics* **10**, 015003–015003 (2023).

35. Lauer, V. New approach to optical diffraction tomography yielding a vector equation of diffraction tomography and a novel tomographic microscope. *J. Microsc.* **205**, 165–176 (2002).

36. Choi, W. *et al.* Tomographic phase microscopy. *Nat. Methods* **4**, 717–719 (2007).

37. Debailleul, M., Georges, V., Simon, B., Morin, R. & Haeberlé, O. High-resolution three-dimensional tomographic diffractive microscopy of transparent inorganic and biological samples. *Opt. Lett.* **34**, 79 (2009).

38. Sung, Y. *et al.* Optical diffraction tomography for high resolution live cell imaging. *Opt Express* **17**, 266 (2009).

39. Cotte, Y. *et al.* Marker-free phase nanoscopy. *Nat Photonics* **7**, 113–117 (2013).

40. Park, Y., Depeursinge, C. & Popescu, G. Quantitative phase imaging in biomedicine. *Nat Photonics* **12**, 578–589 (2018).

41. Balasubramani, V. *et al.* Holographic tomography: techniques and biomedical applications [Invited]. *Appl. Opt.* **60**, B65 (2021).

42. Toy, M. F., Vatandaslar, B. K. & Kerman, B. E. Refractive index tomography of myelinating glial cells. *Quantitative Phase Imaging V* **10887**, 1088713-1088713–5 (2019).

43. Miron, V. E. *et al.* M2 microglia and macrophages drive oligodendrocyte differentiation during CNS remyelination. *Nat Neurosci* **16**, 1211–1218 (2013).

44. Zheng, J., Sun, X., Ma, C., Li, B. & Luo, F. Voluntary wheel running promotes myelination in the motor cortex through Wnt signaling in mice. *Mol. Brain* **12**, 85 (2019).

45. Xiong, H., Zhou, Z., Wu, Z., Feng, Y. & Xie, F. BALB/c mice infected with Angiostrongylus cantonensis: A new model for demyelination in the brain. *Anatomical Rec* **304**, 1084–1093 (2021).

46. Sahel, A. *et al.* Alteration of synaptic connectivity of oligodendrocyte precursor cells following demyelination. *Front Cell Neurosci* **9**, 77 (2015).

47. Zawadzka, M. *et al.* CNS-resident glial progenitor/stem cells produce schwann cells as well as oligodendrocytes during repair of CNS demyelination. *Cell Stem Cell* **6**, 578–590 (2010).

48. Barnes-Vélez, J. A., Yasar, F. B. A. & Hu, J. Myelin lipid metabolism and its role in myelination and myelin maintenance. *Innovation* **4**, 100360 (2023).

49. Kister, A. & Kister, I. Overview of myelin, major myelin lipids, and myelin-associated proteins. *Front. Chem.* **10**, 1041961 (2023).

50. Fu, Y., Talavage, T. M. & Cheng, J.-X. New imaging techniques in the diagnosis of multiple sclerosis. *Expert. Opin. Méd. Diagn.* **2**, 1055–1065 (2008).

51. Buttigieg, E., Scheller, A., Waly, B. E., Kirchhoff, F. & Debarbieux, F. Contribution of intravital neuroimaging to study animal models of multiple sclerosis. *Neurotherapeutics* **20**, 22–38 (2023).

52. Kaiser, T. *et al.* MyelTracer: A semi-automated software for myelin g-ratio quantification. *eNeuro* **8**, ENEURO.0558-20.2021 (2021).

53. Nave, K.-A. & Werner, H. B. Ensheathment and myelination of axons: evolution of glial functions. *Annu. Rev. Neurosci.* **44**, 1–23 (2021).

54. Benninger, Y. *et al.* β1-Integrin signaling mediates premyelinating oligodendrocyte survival but is not required for CNS myelination and remyelination. *J Neurosci* **26**, 7665–7673 (2006).

55. Stikov, N. et al. In vivo histology of the myelin g-ratio with magnetic resonance imaging. NeuroImage 118, 397–405 (2015).

56. Campbell, J. S. W. et al. Promise and pitfalls of g-ratio estimation with MRI. NeuroImage 182, 80–96 (2018).

57. Mohammadi, S. & Callaghan, M. F. Towards in vivo g-ratio mapping using MRI: Unifying myelin and diffusion imaging. J. Neurosci. Methods 348, 108990 (2021).

58. Sele, M. *et al.* Optimization of ultrastructural preservation of human brain for transmission electron microscopy after long post-mortem intervals. Acta Neuropathologica Communications 7, 144 (2019).

59. Baczewska, M., Eder, K., Ketelhut, S., Kemper, B. & Kujawińska, M. Refractive index changes of cells and cellular compartments upon paraformaldehyde fixation acquired by tomographic phase microscopy. Cytometry Part A 99(4), 388–398 (2021).

60. Wehrl, H. F., Bezrukov, I., Wiehr, S., Lehnhoff, M., Fuchs, K., Mannheim, J. G., Quintanilla-Martinez, L., Kohlhofer, U., Kneilling, M., Pichler, B. J. & Sauter, A. W. Assessment of murine brain tissue shrinkage caused by different histological fixatives using magnetic resonance and computed tomography imaging. Histol. Histopathol. 30(5), 601–613 (2015).

61. de Campos Vidal, B., Mello, M. L. S., Caseiro-Filho, A. C. & Godo, C. Anisotropic properties of the myelin sheath. Acta Histochemica 66(1), 32–39 (1980).

62. Dougherty, J. D., Zhang, J., Feng, H., Gong, S. & Heintz, N. Mouse transgenesis in a single locus with independent regulation for multiple fluorophores. *Plos One* **7**, e40511 (2012).

63. Paxinos, G. & Franklin, K. B. J. *The Mouse Brain in Stereotaxic Coordinates*. (Academic Press, San Diego, 2001).

64. Schindelin, J. *et al.* Fiji: an open-source platform for biological-image analysis. *Nat. Methods* **9**, 676–82 (2012).

65. Cuche, E., Marquet, P. & Depeursinge, C. Simultaneous amplitude-contrast and quantitative phase-contrast microscopy by numerical reconstruction of Fresnel off-axis holograms. *Appl. Opt.* **38**, 6994 (1999).

66. Colomb, T. *et al.* Automatic procedure for aberration compensation in digital holographic microscopy and applications to specimen shape compensation. *Appl. Opt.* **45**, 851 (2006).